Terahertz high-sensitivity SIS mixer based on Nb-AlN-NbN hybrid superconducting tunnel junctions

Bo-Liang Liu(刘博梁), Dong Liu(刘冬), MingYao(姚明), Jun-Da Jin(金骏达), Zheng Wang(王争), JingLi(李婧), Sheng-Cai Shi(史生才), Artem Chekushkin, Michael Fominsky, Lyudmila Filippenko, and ValeryKoshelets

Citation: Chin. Phys. B, 2024, 33 (**5**): 058501. DOI: 10.1088/1674-1056/ad2bf7
Journal homepage: http://cpb.iphy.ac.cn; http://iopscience.iop.org/cpb

What follows is a list of articles you may be interested in

Current oscillation in GaN-HEMTs with p-GaN islands buried layer for terahertz applications

Wen-Lu Yang(杨文璐), Lin-An Yang(杨林安), Fei-Xiang Shen(申飞翔), Hao Zou(邹浩), Yang Li(李杨), Xiao-Hua Ma(马晓华), and Yue Hao(郝跃)
Chin. Phys. B, 2022, 31 (**5**): 058505. DOI: 10.1088/1674-1056/ac2b1f

Noise temperature distribution of superconducting hot electron bolometer mixers

Kang-Min Zhou(周康敏), Wei Miao(缪巍), Yue Geng(耿悦), Yan Delorme, Wen Zhang(张文), Yuan Ren(任远), Kun Zhang(张坤), Sheng-Cai Shi(史生才)
Chin. Phys. B, 2020, 29 (**5**): 058505. DOI: 10.1088/1674-1056/ab81f9

The origin of distorted intensity pattern sensed by a lens and antenna coupled AlGaN/GaN-HEMT terahertz detector

Xiang Li(李想), Jian-Dong Sun(孙建东), Hong-Juan Huang(黄宏娟), Zhi-Peng Zhang(张志鹏), Lin Jin(靳琳), Yun-Fei Sun(孙云飞), V V Popov, Hua Qin(秦华)
Chin. Phys. B, 2019, 28 (**11**): 118502. DOI: 10.1088/1674-1056/ab44ac

Integration of a field-effect-transistor terahertz detector with a diagonal horn antenna

Xiang Li(李想), Jian-dong Sun(孙建东), Zhi-peng Zhang(张志鹏), V V Popov, Hua Qin(秦华)
Chin. Phys. B, 2018, 27 (**6**): 068506. DOI: 10.1088/1674-1056/27/6/068506

Mapping an on-chip terahertz antenna by a scanning near-field probe and a fixed field-effect transistor

Lü Li (吕利), Sun Jian-Dong (孙建东), Roger A. Lewis, Sun Yun-Fei (孙云飞), Wu Dong-Min (吴东岷), Cai Yong (蔡勇), Qin Hua (秦华)
Chin. Phys. B, 2015, 24 (**2**): 028504. DOI: 10.1088/1674-1056/24/2/028504

Terahertz high-sensitivity SIS mixer based on Nb–AlN–NbN hybrid superconducting tunnel junctions

Bo-Liang Liu(刘博梁)[1,2], Dong Liu(刘冬)[1,2,†], Ming Yao(姚明)[1], Jun-Da Jin(金骏达)[1], Zheng Wang(王争)[1,2], Jing Li(李婧)[1,2], Sheng-Cai Shi(史生才)[1,2,‡], Artem Chekushkin[3], Michael Fominsky[3], Lyudmila Filippenko[3], and Valery Koshelets[3]

[1] *Purple Mountain Observatory, Chinese Academy of Sciences, Nanjing* 210023, *China*
[2] *School of Astronomy and Space Sciences, University of Science and Technology of China, Hefei* 230026, *China*
[3] *Kotel'nikov Institute of Radio Engineering and Electronics, Russian Academy of Sciences, Moscow* 125009, *Russia*

(Received 18 January 2024; revised manuscript received 7 February 2024; accepted manuscript online 22 February 2024)

The terahertz band, a unique segment of the electromagnetic spectrum, is crucial for observing the cold, dark universe and plays a pivotal role in cutting-edge scientific research, including the study of cosmic environments that support life and imaging black holes. High-sensitivity superconductor–insulator–superconductor (SIS) mixers are essential detectors for terahertz astronomical telescopes and interferometric arrays. Compared to the commonly used classical Nb/AlO$_x$/Nb superconducting tunnel junction, the Nb/AlN/NbN hybrid superconducting tunnel junction has a higher energy gap voltage and can achieve a higher critical current density. This makes it particularly promising for the development of ultra-wideband, high-sensitivity coherent detectors or mixers in various scientific research fields. In this paper, we present a superconducting SIS mixer based on Nb/AlN/NbN parallel-connected twin junctions (PCTJ), which has a bandwidth extending up to 490 GHz–720 GHz. The best achieved double-sideband (DSB) noise temperature (sensitivity) is below three times the quantum noise level.

Keywords: SIS mixer, terahertz, gap voltage, critical current density, hybrid superconducting tunnel junction

PACS: 85.25.Pb, 85.25.Am, 95.55.Jz **DOI:** 10.1088/1674-1056/ad2bf7

1. Introduction

The terahertz band, spanning from 0.1 THz to 10 THz, represents a distinctive electromagnetic spectrum ideal for observing the cold and dark universe. This band is rich in molecular atomic lines and holds significant scientific value for investigations into black holes, the origins and evolution of galaxies, and the potential for life in the universe.[1] The high-sensitivity superconducting superconductor–insulator–superconductor (SIS) mixer serves as a pivotal detector within the terahertz band astronomical telescope. It stands out as the most sensitive detector below 1 THz and plays a crucial role in numerous globally recognized observation apparatuses, such as SMA (Submillimeter Array),[2] ALMA (Atacama Large Millimeter/submillimeter Array)[3] and Herschel HIFI (Heterodyne Instrument for the Far-Infrared).[4] The prevalent Nb/AlO$_x$/Nb SIS mixers reach a noise performance of $3h\nu/k_{\rm B}$.[5] Notably, exceptional submillimeter wave observation stations are located in Antarctica Dome A (Kunlun Station) and the Qinghai-Tibet Plateau area,[6,7] highlighting the promising future applications of superconducting SIS mixers in telescope construction.

SIS mixer with wider frequency coverage (RF bandwidth) can enhance the observation efficiency of astronomical telescopes. Theoretically, the bandwidth of the SIS mixer is contingent upon its energy gap voltage ($V_{\rm gap}$) and critical current density ($J_{\rm c}$).[8] A larger RF bandwidth requires higher critical current density, while a higher gap voltage helps move the mixer operating point away from the influence of the Josephson effect, improving the sensitivity and stability of the mixer. The widely adopted Nb/AlO$_x$/Nb superconducting tunnel junction boasts a well-established fabrication process. Yet, achieving high quality factor tunnel junctions becomes challenging when the critical current density exceeds 10 kA/cm^2. On the other hand, the NbN/AlN/NbN superconducting tunnel junction, characterized by its higher energy gap voltage and superconducting transition temperature ($T_{\rm C}$), can operates within the temperature range of 8 K–10 K, which makes it particularly advantageous for space applications where stringent control over receiver power consumption is essential.[9] However, its disadvantage is the lower coherence length of the NbN material, which requires a thinner potential barrier layer to achieve the same critical current density. Additionally, perforation structures are prone to formation in the potential barrier layer, leading to the multiple Andreev reflection (MAR) effect. This phenomenon compromises the noise performance of the superconducting mixer and complicates the fabrication of high-quality factor devices. In contrast, the Nb/AlN/NbN hybrid superconducting tunnel junction integrates the estab-

[†]Corresponding author. E-mail: dliu@pmo.ac.cn
[‡]Corresponding author. E-mail: scshi@pmo.ac.cn

lished fabrication process of the Nb superconducting tunnel junction with the high energy gap voltage of the NbN superconducting tunnel junction. This combination achieves a high-quality factor, even when the critical current density exceeds 10 kA/cm^2.[10]

In this study, we designed, fabricated, and characterized a superconducting SIS mixer. Different with Nb/AlO$_x$/Nb SIS mixers, the mixer was based on Nb/AlN/NbN parallel-connected twin junctions (PCTJ) integrated with NbTiN/SiO$_2$/Al microstrip circuit. By optimizing the dimensions of the junction capacitance tuning and feed point impedance matching circuit, as well as accurately defining the tunnel junctions, we achieved wideband performance of the mixer at a critical current density of 15 kA/cm^2. We analyzed the effects of bias voltage, intermediate frequency (IF), and local oscillator (LO) amplitude-modulated (AM) noise on the mixer's performance. Additionally, we evaluated the mixer's performance within the LO frequency range of 490 GHz–720 GHz, where the double-sideband (DSB) noise temperatures (sensitivity) are below three times the quantum noise ($< 3h\nu/k_B$, comparable to the mixers with Nb/AlO$_x$/Nb junction) at the optimum frequency.

2. Design and fabrication

2.1. Design of waveguide-to-microstrip transition

The superconducting mixer incorporates a waveguide-type structure, with the design of the mixer's waveguide-to-microstrip transition illustrated in Fig. 1(a). While designing a reduced-height waveguide with a back short-circuit cavity typically facilitates achieving low input impedance and broad working bandwidth, to mitigate processing difficulties and reduce additional loss due to surface resistance and waveguide roughness, we opted for a WR-1.5 (381 μm×191 μm) full-height waveguide without a back short-circuit cavity. The chip was positioned within the mounting slot, with the feed point oriented towards the waveguide's center. A low pass filter was implemented on the chip to inhibit RF signal leakage, ensuring that the IF signal transmitted via heterodyne mixing reached the port. Additional losses arise from the fundamental mode propagating to the IF port and higher order modes not transmitting within the chip's mounting slot. The manifestation of higher order modes is contingent upon the dielectric constant, substrate thickness, and microstrip width; thus, we utilized a quartz substrate with a moderate dielectric constant of 3.78. Maintaining consistent substrate thickness, we employed a combination of a resonant choke filter, *i.e.*, termed a hammer filter and conventional high and low impedance line choke filters, to more effectively suppress higher order modes and prevent fundamental mode leakage into the IF port. High frequency electromagnetic field simulation software (HFSS) simulations revealed that with a chip thickness of 50 μm, width of 120 μm, length of 1500 μm, chip mounting slot width of 130 μm, and height of 117 μm, optimizing butterfly antenna structure and choke circuit size, the input return loss at the feed point in the frequency band of 500 GHz–750 GHz is depicted in Fig. 1(b). Additionally, the complex plane input impedance normalized to 40 Ω is presented as an inserted Smith chart.

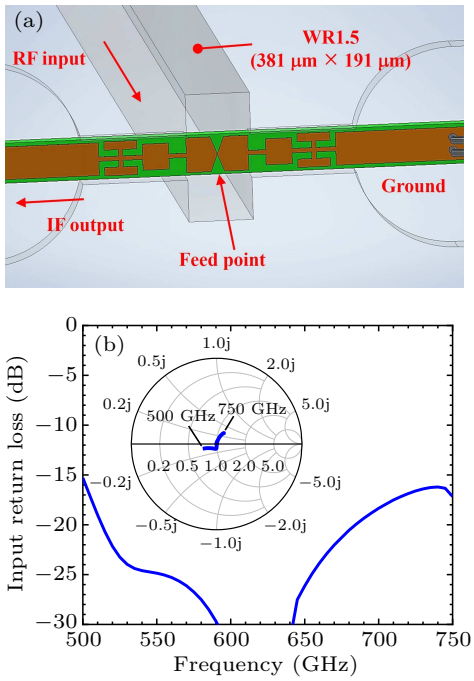

Fig. 1. (a) Schematic layout of probe and choke filter on quartz substrate. (b) The modeled (HFSS) input return loss and input impedance in the complex plane from 500 GHz to 750 GHz.

2.2. Design of tunnel junction and tuning circuit

The SIS mixer utilizes a PCTJ structure, consisting of two superconducting tunnel junctions interconnected by a microstrip line inductance. The PCTJ structure offers the benefits of a larger junction size and reduced RF resistance.[11,12] The inter-junction capacitance tuning and impedance transformation between the tunnel junction and the feed point are achieved using a superconducting microstrip circuit. The center frequency of this specially designed tuning circuit is 625 GHz. Figure 2(a) depicts an optical microscope image illustrating the waveguide-to-microstrip transition and tuning circuit of the chip, while figure 2(b) presents a schematic diagram depicting the chip's cross-sectional structure.

To achieve operation across a broad frequency band, the critical current density of the tunnel junction is configured at 15 kA/cm^2. The area of the tunnel junction measures 1 μm^2, with the normal state resistance (R_n) and geometric capacitance (C_j) being 11 Ω and 95 fF respectively. Assuming an I_cR_n product of 1.65 mV, the characteristic capacitance (C_s) is determined to be 95 fF/μm^2. The tunnel junction is characterized as an Nb/AlN/NbN hybrid junction, featuring a base electrode composed of an 80-nm thick Nb on NbTiN, a middle layer of 7 nm of Al, discharge nitridation in pure nitrogen,

resulting in 1 nm–1.2 nm of AlN, and a top electrode made of 80-nm thick NbN.

The microstrip line is constructed from NbTiN/SiO_2/Al. The NbTiN layer, situated on a quartz dielectric with a thickness of 325 nm, operates at a critical temperature of 14.4 K in the design. It exhibits a resistivity of 110 μΩ·cm at 20 K. The wiring layer, Al, has a thickness of 400 nm and is assumed to have a resistivity of 0.4 μΩ·cm at 4 K. The intermediate dielectric, SiO_2, has a thickness of 250 nm and a permittivity of 3.8. By employing these parameters, the surface impedance of the NbTiN film was estimated using the Mattis–Bardeen theory to calculate the penetration depth.[13] The impedance transformation from the PCTJ impedance (5.5 Ω) to the feed point impedance (40 Ω) was accomplished using a quarter-wavelength impedance transformer.

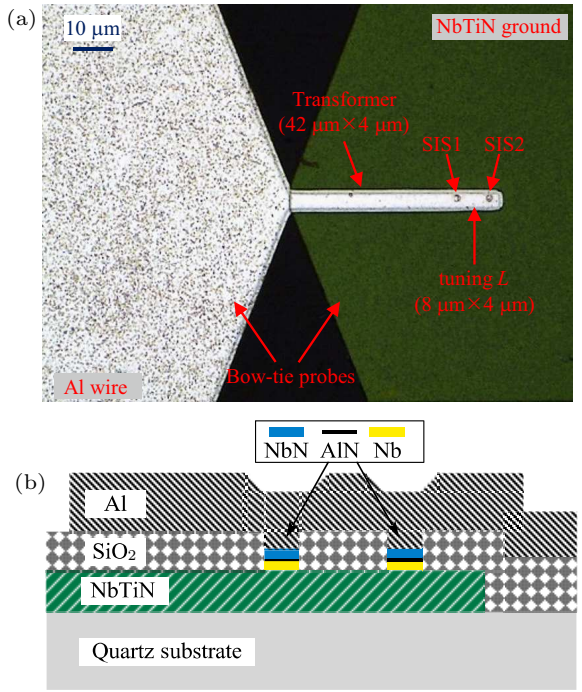

Fig. 2. (a) An optical microscope image of the twin-junction circuit, optimized dimensions of the tuning circuit of PCTJ and feed point impedance matching circuit are labeled. (b) The cross-sectional structure of the twin-junction circuit.

The dimensions of the PCTJ tuning circuit and the feed point embedded impedance matching circuit are optimized using Tucker quantum mixing theory simulations,[8] as depicted in Fig. 2(a). Figure 3(a) illustrates the simulated DSB frequency conversion gain and noise temperature of the mixer across the frequency range of 550 GHz–720 GHz. The frequency conversion gain is approximately 0 dB, while the noise temperature ranges from 25 K to 35 K. Figure 3(b) presents the calculated power coupling efficiency between the feed point and the superconducting tunnel junction. The curve with a red band and a blank square represents the coupling efficiency of SIS1, the curve with a blue band and a blank triangle signifies the coupling efficiency of SIS2, and the curve with a pink band and a solid circle point indicates the total coupling efficiency of the PCTJ. Notably, the overall coupling efficiency exceeds 70% across the 550 GHz–720 GHz band.

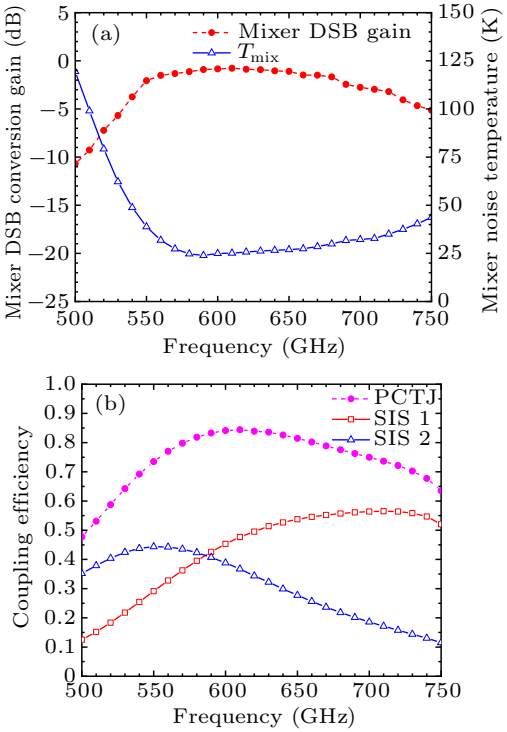

Fig. 3. (a) Simulated mixer DSB conversion gain and mixer noise temperature. (b) Power coupling efficiency between SIS tunnel junctions and feed point.

2.3. Mixer fabrication

The chip was fabricated in an oil-free ultrahigh vacuum sputtering system, which was equipped with five-inch DC and RF magnetron sources, an ion gun, and a grounded water-cooled substrate stage.[14] Quartz wafers were attached to a copper chuck using vacuum grease and then placed on the substrate stage. Initially, 325-nm thick NbTiN films were deposited on fused silica substrates using DC magnetron sputtering of an NbTi target in a mixture of Ar and 9% N_2 atmosphere at room temperature. The NbTiN bottom electrode pattern was created using reactive ion etching (RIE). The SIS tunnel junction is composed of three layers of Nb/AlN/NbN. After depositing the Nb-based electrode and one layer of Al by DC magnetron sputtering, an aluminum nitride tunnel barrier was immediately grown using RF magnetron discharge. The sample was fixed on the grounded substrate stage at a temperature of 20 °C, positioned directly above the 5-inch (1 inch = 2.54 cm) aluminum magnetron RF source, with the holder placed 14 cm away from the RF source. To produce triple-layer films with a high critical current density, we initiated a plasma discharge with a power density of 0.7 W/cm^2 at a nitrogen pressure of 4.5 Pa for approximately 40 s. Subsequently, NbN thin films were deposited using DC reactive magnetron sputtering at ambient temperature with a power density of 1.8 W/cm^2, employing a gas mixture of Ar and 9% N_2. SIS junctions with an area of approximately 1 μm^2 were

fabricated on Nb/AlN/NbN tri-layer films using photolithography, RIE for etching Nb and NbN, and ion etching to physically remove Al–AlN, and anodization technique to prevent short connection between side part of SIS-junction and aluminum electrode.[15] The dielectric layer for the junction insulation consists of 250 nm of SiO_2, which is defined by a self-aligned lift-off process. Finally, top microstrip electrodes, 400 nm in thickness, are deposited using DC magnetron sputtering and defined through a lift-off process. Following this, the quartz substrate is reduced to a thickness of 50 μm through mechanical polishing.

3. Characterization results and discussion

3.1. Measurement setup

The performance characterization of the mixer was conducted in a 4-K liquid helium Gifford–McMahon cycle cryosystem, utilizing the standard Y-factor method. This involved both a room temperature hot (295 K) load and a liquid nitrogen immersion cold (77 K) load. Figure 4 presents the system block diagram for the mixer's performance characterization. The LO and RF signals were coupled via a 12.5-μm Mylar beam-splitter, subsequently entering the dewar through a 500-μm thick HDPE vacuum window and a 100-μm thick Zitex IR filter situated at the 50-K window. These were then coupled to the diagonal horn using a parabolic reflector. The mixer's output IF signal was amplified by a cryogenic low noise amplifier (CLNA), exhibiting a noise of 4 K within the range of 0.3 GHz–14 GHz. This was then routed to a room temperature IF amplification circuit for further amplification, and subsequently recorded either through bandpass filters with a power meter or directly with a spectrum analyzer. Josephson noise was effectively suppressed by a pair of fixed permanent magnets.

The reference signal of the LO was generated using a commercial analog signal generator E8257D, which can reach frequencies up to 20 GHz. The signal was then processed through a YIG tunable bandpass filter to reduce the impact of the fundamental signal on the AM noise of the LO. Following this, the frequency was multiplied by a 36-fold chain, consisting of an active doubler followed by a power amplifier, and then another active doubler followed by two passive triplers. This process was carried out by VDI company to ensure that the LO frequency ranged from 520 GHz to 720 GHz.

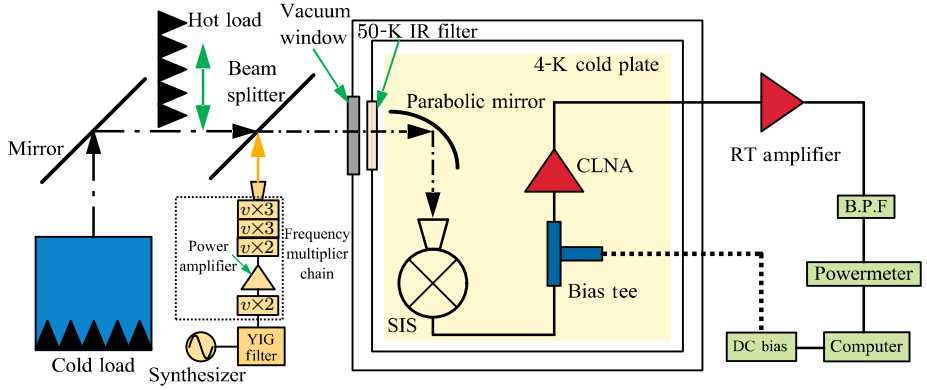

Fig. 4. Schematic diagram of mixer's performance measurement setup.

3.2. System performance

The mixer exhibits an outstanding I–V characteristic curve, with a resistance ratio (R_{sg}/R_n) from sub-gap to normal state reaching up to 32. Figure 5(a) illustrates the measured I–V characteristic curves of the SIS mixer both with and without a 620-GHz LO signal. The energy gap voltage is recorded as 3.15 mV, while the PCTJ's normal state resistance measures at 7.6 Ω, slightly exceeding the designed value of 5.5 Ω. This discrepancy may be attributed to either the actual tunneling junction area or the critical current density being relatively small. Upon introducing an LO signal, photon assisted quasi-particle steps become distinctly visible. It should be highlighted that when a 620-GHz LO signal is inputted, photon steps originating from the negative gap voltage generated by nonlinearity emerge at 1.9 mV ($-V_{gap}+2h\nu/e$). Figure 5(a) also presents the variation curve of the IF output power response in relation to bias voltage when a cold/hot load radiation signal is introduced. The system's DSB noise temperature (T_{rx}) variation as a function of bias voltage, calculated using the Y-factor, is depicted in Fig. 5(b). The optimal noise temperature approximates 125 K when the LO current surpasses the dark current at 2 mV by 55 μA.

Furthermore, the impact of the first and second Shapiro steps ($S_n = nh\nu/2e$), which result from the incomplete suppression of the Josephson effect, is evident in the noise temperature at the corresponding bias voltage point. The input load equivalent temperatures (T_h, T_c) are calculated using the Callen & Welton formula. Vacuum zero-point fluctuation noises are included in the blackbody radiation temperature, which approximates the Rayleigh–Jeans limit at the test frequency.[16,17]

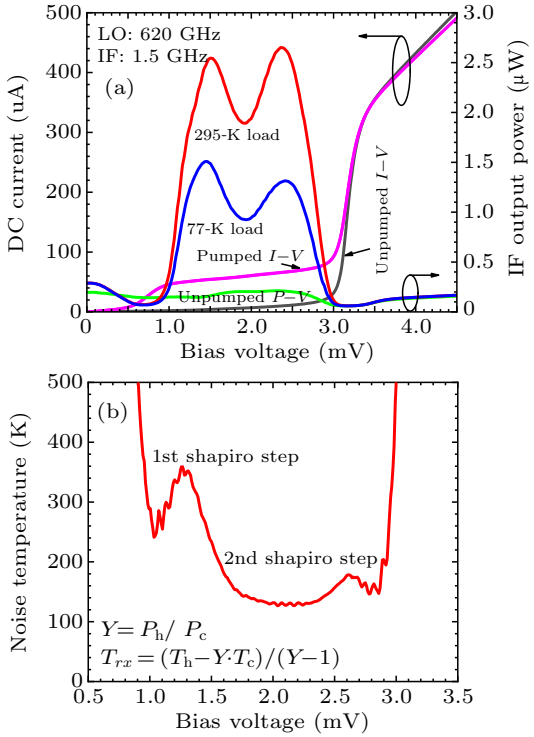

Fig. 5. (a) The left axis shows the DC I–V curves, the grey curve is unpumped I–V, the pink curve is pumped I–V, the right axis shows the IF output power varies with bias voltage, the green curve is unpumped output power, the red and blue curve are output power corresponding to hot load and cold load. (b) The DSB receiver noise temperature varies with bias voltage, two Shapiro steps are clearly seen originating from insufficient suppression of Josephson effect.

3.3. IF performance and AM noise of LO

The IF link of the receiver system comprises a wideband bias circuit (Bias-T), a CLNA operating within the range of 0.3 GHz–14 GHz, and a room temperature low noise amplifier (RLNA) functioning in 0.1 GHz–20 GHz. A spectrum analyzer is employed to document the IF output spectrum upon switching between cold and hot input signals. Subsequently, the variation in DSB noise temperature relative to the IF is calculated. By modulating the LO frequency, we ascertain the comprehensive IF bandwidth performance of the superconducting mixer spanning 0.3 GHz–14 GHz. Figure 6(a) illustrates the two-dimensional noise temperature distribution, depicting the system noise temperature fluctuation with respect to the IF within the band of 570 GHz–640 GHz. Here, the horizontal axis represents the IF, while the vertical axis denotes the LO frequency, with color indicative of noise temperature. Owing to the absence of an isolator, impedance mismatch between the mixer output and CLNA input induce a degree of standing wave, particularly pronounced at elevated frequencies. Notably, at lower IF (marked by the red circle), additional noise stemming from LO amplitude modulation noise[18,19] elevates the system noise temperature in these regions. By incorporating YIG tunable bandpass filters between signal generator and frequency multiplier chains, we enhance the signal-to-noise ratio for fundamental frequency signals, mitigate additional AM noise introduced by LO, and achieve the IF bandwidth performance distribution depicted in Fig. 6(b). This figure underscores a marked suppression effect; notably, when disregarding the impact of standing waves, the system's performance remains consistent across the IF spectrum. The region delineated by the purple circles represent a region of pronounced water vapor absorption proximate to the peak frequency of 557 GHz. This phenomenon results in an augmented signal transmission loss, consequently leading to an elevated system noise temperature.

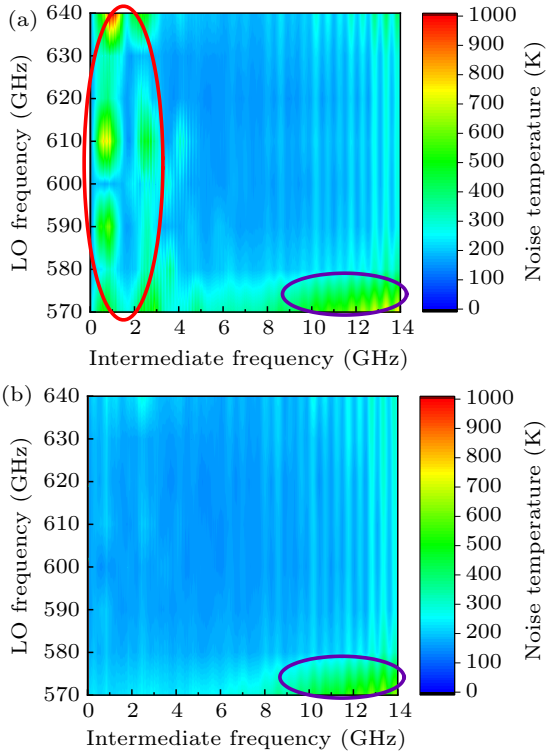

Fig. 6. Comparison of DSB receiver noise temperature vary with LO frequency and IF without (a) and with (b) YIG tunable bandpass filter between signal generator and frequency multiplier chain, different noise temperatures show different colors, seen as right color bar. The periodic fluctuation caused by standing wave is particularly obvious at high IF frequency. The purple circles indicate the increased noise temperature caused by water vapor absorption at 557 GHz.

3.4. Mixer performance

The red curve in Fig. 7 represents the double-sideband (DSB) noise temperature of the receiver across the frequency range of 490 GHz–720 GHz. As shown, the mixer operates at a center frequency of 610 GHz, with a fractional bandwidth of 38%. At this optimal frequency point, the receiver noise temperature reaches $5h\nu/k_B$. Furthermore, it is observed that the receiver noise temperature escalates due to the pronounced water vapor absorption effect within the frequency range of 540 GHz–575 GHz. The contribution of each component of the receiver system to the noise temperature can be articulated using Eq. (1), where T_{RF} represents RF noise temperature, G_{RF} denotes front-end RF gain, T_m signifies mixer intrinsic noise temperature, G_m represents mixer frequency conversion gain, and T_{IF} indicates IF noise temperature.

$$T_{rx} = T_{RF} + \frac{1}{G_{RF}}\left(T_m + \frac{T_{IF}}{G_m}\right). \tag{1}$$

As illustrated in Fig. 4, the RF noise predominantly originates from the losses of optical components within the test system. These include the beam-splitter film (Mylar), vacuum window (HDPE), and infrared filter (Zitex). The gain G of these components was ascertained using an ADVANTEST (TAS7500SP model) time domain spectrometer test,[20] yielding values of -0.1 dB, -0.45 dB, and -0.31 dB at 610 GHz, respectively. The equivalent input noise temperature associated with this gain is denoted as $T_{\rm eq} = T_{\rm cw}(T)(1-G)/G$, $T_{\rm cw}$ represents Callen & Welton's equivalent temperature. The cumulative RF input noise is derived by cascading the contributions of each individual component.

The $T_{\rm IF}$ of the experimental system is less than 10 K, indicating that the system's corrected DSB noise temperature is dominated by the mixer itself, as shown in the green curve in Fig. 7, which is less than 150 K in the range of 510 GHz–675 GHz and a minimum value of 75 K at 610 GHz. Considering that there might be some material gain errors due to testing near the lower limit of TDS model's operating frequency range, we suggest incorporating an estimated correction error bar of approximately 20 K to account for this potential discrepancy. However, it is evident that the system DSB noise temperature, post-correction for the front-end component optical loss, remains below $3h\nu/k_{\rm B}$ near the optimal frequency. As only the loss of window materials was corrected, the impact of water vapor absorption in the actual optical path remains observable.

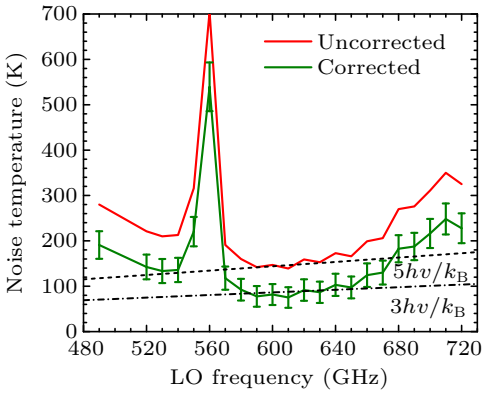

Fig. 7. Uncorrected and corrected DSB receiver noise temperature at 4 K. A vacuum window of 500-μm HDPE and beam splitter of 12.5-μm Mylar film and IR filter of 100-μm Zitex were used for the measurement.

When the mixer is integrated into a future practical telescope receiver, RF components, such as front-end optical windows, will be carefully optimized. This optimization will involve implementing targeted antireflection coatings and other measures aimed at minimizing additional losses, thereby ensuring superior receiver performance metrics.

4. Conclusion

In summary, we have successfully designed, fabricated, and characterized a superconducting SIS mixer based on the Nb/AlN/NbN PCTJ integrated with NbTiN/SiO_2/Al microstrip circuit. The mixer's excellent performance across a wide frequency range of 490 GHz–720 GHz can be attributed to its precise design and well-established fabrication process. This significantly improves efficiency in astronomical observations. The minimum corrected DSB noise temperature (sensitivity) at the optimal frequency point of 610 GHz is 75 K, which is less than three times the quantum noise ($< 3h\nu/k_{\rm B}$). These exceptional THz SIS mixers are promising candidates for the future construction of submillimeter telescopes in the Antarctic Dome A region and the Qinghai–Tibet Plateau in China.

Acknowledgements

Project supported in part by the National Key Research and Development Program of China (Grant Nos. 2023YFA1608201 and 2023YFF0722301) and the National Natural Science Foundation of China (Grant Nos. 11925304, 12020101002, 12333013, 12273119, and 12103093). The samples fabrication was supported by grant from the Russian Science Foundation (Grant No. 23-79-00019).

References

[1] Phillips T G and Keene J 1992 *Proc. IEEE* **80** 1662
[2] Ho P T P, Moran J M and Lo K Y 2004 *Astrophys. J.* **616** L1
[3] Wootten B A and Thompson A R 2009 *Proc. IEEE* **97** 1463
[4] De Graauw T, Helmich F P, Phillips T G, *et al.* 2010 *Astron. Astrophys.* **518** L6
[5] Zmuidzinas J and Richards P L 2004 *Proc. IEEE* **92** 1597
[6] Shi S C, Paine S, Yao Q J, Lin Z H, Li X X, Duan W Y, Matsuo H, Zhang Q Z, Yang J, Ashley M C B, Shang Z H and Hu Z W 2016 *Nat. Astron.* **1** 0001
[7] Lin Z H, Miao W, Yao M, Wu F, Yao Q J, Fan B W, Liu B L and Shi S C 2023 *Sci. China-Phys. Mech. Astron* **66** 299515
[8] Tucker J R and Feldman M J 1985 *Rev. Mod. Phys.* **57** 1055
[9] Li J, Takeda M, Wang Z, Shi S C and Yang J 2008 *Appl. Phys. Lett.* **92** 222504
[10] Torgashin M Y, Koshelets V P, Dmitriev P N, Ermakov A B, Filippenko L V and Yagoubov P A 2007 *IEEE Trans. Appl. Supercond.* **17** 379
[11] Shi S C and Noguchi T 1998 *IEICE Trans. Electron.* **81** 1584
[12] Zmuidzinas J, LeDuc H G, Stern J A and Cypher S R 1994 *IEEE Trans. Microw. Theory* **42** 698
[13] Mattis D C and Bardeen J 1958 *Phys. Rev.* **111** 412
[14] Dmitriev P N, Lapitskaya I L, Filippenko L V, Ermakov A B, Shitov S V, Prokopenko G V, Kovtonyuk S A and Koshelets V P 2003 *IEEE Trans. Appl. Supercond.* **13** 107
[15] Fominsky M Y, Filippenko L V, Chekushkin A M, Dmitriev P N and Koshelets V P 2021 *Electronics* **10** 2944
[16] Kerr A R, Feldman M J and Pan S K 1997 *Proceedings of the 8th International Symposium on Space Terahertz Technology*, March 25–27, 1997, Massachusetts, USA, p. 101
[17] Callen H B and Welton T 1951 *Phys. Rev.* **83** 34
[18] Erickson N 2004 *Proceedings of the 15th International Symposium on Space Terahertz Technology,* April 27–29, 2004, Massachusetts, USA, p. 135
[19] Bryerton E W and Hesler J 2008 *Proceedings of the 19th International Symposium on Space Terahertz Technology,* April 28–30, 2008, Groningen, The Netherlands, p. 498
[20] Li H H, Lv W T, Liu D, Fan B W, Yao M, Liu B L, Li J and Shi S C 2019 *Infrared, Millimeter-Wave, and Terahertz Technologies VI. SPIE*, October 20–23, 2019, Hangzhou, China, p. 132